

Wafer-scale fabrication of 2D van der Waals heterojunctions for efficient and broadband photodetection

*Jian Yuan^{†, //} Tian Sun,^{†, //} Zhixin Hu^{‡, //} Wenzhi Yu,[†] Weiliang Ma,[†] Kai Zhang[⊥], Baoquan Sun,[†] Shu Ping Lau,[#] Qiaoliang Bao,[§] Shenghuang Lin^{#, *} and Shaojuan Li^{†, *}*

[†]Institute of Functional Nano and Soft Materials (FUNSOM), Jiangsu Key Laboratory for Carbon-Based Functional Materials and Devices, Collaborative Innovation Center of Suzhou Nano Science and Technology, and Joint International Research Laboratory of Carbon-Based Functional Materials and Devices, Soochow University, Suzhou 215123, People's Republic of China

[‡]Center for Joint Quantum Studies and Department of Physics, Tianjin University, Tianjin 300350, People's Republic of China

[⊥]*i*-Lab, Suzhou Institute of Nano-Tech and Nano-Bionics, Chinese Academy of Sciences, Suzhou 215123, Jiangsu, People's Republic of China

[#]Department of Applied Physics, The Hong Kong Polytechnic University, Hung Hom, Hong Kong SAR, People's Republic of China

[§]Department of Materials Science and Engineering, and ARC Centre of Excellence in Future Low-Energy Electronics Technologies (FLEET) Monash University, Clayton, Victoria 3800, Australia.

^{//}These authors contributed equally to this work.

*Address correspondence to (S. Lin) shenghuanglinchina@gmail.com and (S. Li) sjli@suda.edu.cn

ABSTRACT

A variety of fabrication methods for van der Waals heterostructures have been demonstrated; however, their wafer-scale deposition remains a challenge. Here we report few-layer van der Waals PtS₂/PtSe₂ heterojunctions fabricated on a 2" SiO₂/Si substrate that is only limited by the size of work chamber of the growth equipment, offering throughputs necessary for practical applications. Theoretical simulation was conducted to gain basic understanding of the electronic properties of the PtS₂/PtSe₂ heterojunctions. Zero-bias photoresponse in the heterojunctions is observed under laser illumination of 405 to 2200 nm wavelengths. The PtS₂/PtSe₂ heterojunctions show excellent characteristics in terms of broadband photoresponse and high quantum efficiency at infrared wavelengths, as well as a fast response speed at the millisecond level. The wafer-scale production of 2D heterojunctions in this work accelerates the possibility of 2D materials for applications in the next-generation energy-efficient electronics.

KEYWORDS: van der Waals heterostructures, wafer-scale fabrication, self-driving operation, photoresponsivity

Heterojunctions, firstly invented in 1963 by Herbert Kroemer¹, have been essential building blocks for electronic and optoelectronic devices in the current semiconductor industry. Uses of such structures have been envisioned in nearly every type of semiconductor devices, including biomedical devices, bipolar transistor, photodiodes, light-emitting diodes, and solar cells. As one of the most important existing optoelectronic devices, the photodiodes obviously play an important role in the applications of video imaging, optical communication, remote control and night vision^{2, 3}. Recent studies have shown that heterostructures based on two-dimensional (2D) materials, which contains atomically sharp interfaces, can indeed be competitive with or even superior to conventional bulk semiconductor based junctions^{4, 5, 6}. Encouragingly, 2D transition metal dichalcogenides (TMDs), one important member from the family of atomically thin van der Waals materials, has been widely studied and proved to be of great potential for the applications of future optoelectronics owing to their outstanding electronic, optical, mechanical properties and the strong light–matter interactions⁷⁻⁹. TMDs have extended bandgap tunability through composition¹⁰, thickness^{11, 12} and possibly even strain control¹³ offering infinite flexibility to design 2D junctions^{4, 14-18}, which has been used in photovoltaics, photodiodes and light emitters^{11, 15, 19}, and could overcome some of the existing problems in conventional junction devices²⁰.

Therefore, driven by the diversity and considerable wide coverage properties of TMDs materials, artificial 2D van der Waals junctions have been fabricated using either homogeneous or heterogeneous 2D materials^{17, 21}. The formation of 2D homojunction can be formed by chemical/gate-induced electrical doping in the same nanoflake which lacks stability or makes device structures complicated^{19, 22, 23}. The fabrication of 2D heterojunctions, however, mainly extends directly to materials produced by exfoliation from the bulk counterpart using a variety of techniques^{6, 17}, but indirectly to those that can be deposited onto targeted substrates with facile control for the practical realization of high-volume manufacturing. Controllable large-scale integration of more than one type of 2D materials onto a single substrate still remains a challenge. Previously, we have demonstrated the scalable production of periodic patterns of few-layer WS₂/MoS₂ heterojunction arrays by a thermal reduction sulfurization process²⁴, however, the TMDs/TMDs heterostructures reported display a spectral response that is mainly limited

to visible wavelengths by the intrinsic bandgap of the constituting materials²⁵.

Recently, the group 10 metal based TMDs have attracted intense interests for the widely tunable bandgap, large electrical conductivity and high air stability, which can well make up the drawbacks of graphene (zero bandgap), other TMDs semiconductors (relatively large bandgap), and black phosphorus (poor air stability). Representative examples of this family are platinum diselenide (PtSe₂) and platinum disulfide (PtS₂) that can be synthesized via a single step, *i.e.* direct selenization (or sulfuration) of the Pt substrate^{25, 26}. Layered PtSe₂ has a tunable bandgap ranging from 1.2 eV (monolayer) to semimetal (bulk)²⁵, while layered PtS₂ has a bandgap that varies from 1.6 eV in monolayer to 0.25 eV in bulk²⁷. The large spread of bandgaps from visible to mid-infrared is similar to that of layered black phosphorus (BP)²⁸, revealing potential for infrared electronic application. Compared to other extensively studied TMDs, such as MoX₂, WX₂ (X is S, Se, or Te) *etc*, field-effect transistors based on PtSe₂ layers exhibit higher mobility at room temperature, suggesting that this material is applicable for high-speed electron transport devices²⁹. Furthermore, few-layer PtSe₂ nanosheets have been used to make infrared photodetectors with good photoresponsivity and fast response²⁹⁻³². Most recently, bilayer PtSe₂ field effect transistors were demonstrated for broadband mid-infrared photodetection with a high photoresponsivity of $\sim 4.5 \text{ AW}^{-1}$ and response speed at the millisecond level³³. Previous research on few-layer PtS₂ phototransistors also demonstrates high photoresponsivity and photoconductive gain due to the existence of trap states³⁴. Although the optoelectronic properties of individual 2D group-10 TMDs have been preliminary studied, the comprehensive study of van der Waals like interlayer coupling of two different group-10 TMDs and their 2D heterojunctions, which can dramatically affect the band-structures and optoelectronic properties of 2D TMDs, are still lacking. By combining their advantages of ultrahigh stability and infrared light absorption, group-10 TMDs based 2D heterojunctions could be promising for low-power and high speed optoelectronic devices at infrared wavelengths.

Herein, we report a simple strategy to create few-layer PtS₂/PtSe₂ heterojunctions on the surfaces of planar substrates to enable wafer-scale manufacturing of 2D heterostructure arrays based on group-10 TMDs. Such 2D heterojunctions can be formed directly through selenization (or sulfuration) of the Pt substrate by changing the Se source from S on the Pt

layer using an ambient pressure conversion process. The coverage, size, and shape of PtS₂/PtSe₂ film can be controlled as desired, and their thicknesses were determined by the thicknesses of the pre-deposited Pt film. Methods based on above process are naturally compatible with modern planar technologies, and they offer throughputs necessary for practical applications. Theoretical simulations were conducted using the Vienna ab initio simulation package to gain basic understanding of the electronic properties of the PtS₂/PtSe₂ heterojunctions. Zero-bias photoresponse in the heterojunctions is observed under laser illuminations of 405 to 2200 nm wavelengths. Upon optical illumination, the PtS₂/PtSe₂ heterostructures show high photoresponsivity and quantum efficiency at infrared wavelengths with lower bounds for the external quantum efficiencies (EQE) being 1.2% at 1064 nm, 0.2% at 1550 nm and 0.05% at 2200 nm , as well as fast response speed at the millisecond level. These heterojunctions show great promise for broad-band photodetection.

RESULTS AND DISSCUSSION

The vertical heterojunction arrays (see Figure 1a and 1b for microscope images) were obtained on an oxide silicon wafer with 300 nm thick silicon dioxide. They consist of few-layer PtS₂ and PtSe₂ films that were synthesized via direct sulfuration or selenization of the Pt substrate by changing the Se source from S on the Pt layer using an ambient pressure conversion process (see Methods for more details). Our fabrication process enables manufacturability of wafer-scale production of 2D heterojunctions for optoelectronic applications, and the maximum sample size obtained in our experiment is up to 2" in diameter limited by the work chamber of the equipment. From the high-resolution optical microscopy images (Figure 1b), we can observe that the PtS₂ and PtSe₂ sheets are well-defined with very uniform contrast, irrespective of single PtS₂ or PtSe₂ sheet or their overlap region, which is attributed to the delicate control of growth process, proper thermal budget and homogeneous thickness of PtS₂ and PtSe₂ sheets. The size of PtS₂ sheets and PtSe₂ sheets were designed to be $100 \times 120 \mu\text{m}^2$ and $100 \times 100 \mu\text{m}^2$, respectively. Atomic force microscopy (AFM) was used to probe the detailed surface morphology and the thicknesses of PtS₂, PtSe₂ sheets, and their vertical heterojunctions (Figure 1c). The AFM height profile indicates that the thickness of PtS₂/PtSe₂ heterojunction is ~ 5.1 nm.

We have also measured the pure PtS₂ and PtSe₂ regions, respectively. The thicknesses of PtS₂ and PtSe₂ are measured to be ~2.5 and ~2.7 nm, corresponding to five layers of PtS₂ and five layers of PtSe₂, respectively²⁵.

Raman spectroscopy was utilized to identify and characterize the obtained PtS₂/PtSe₂ heterojunction films. Figure 1d shows the polarization-dependent Raman spectra of PtS₂/PtSe₂ heterojunction excited by a 633 nm laser. Both the feature peaks of PtS₂ and PtSe₂ are observed in the spectra. The two feature peaks at ~176 cm⁻¹ and ~210 cm⁻¹ correspond to the E_g and A_{1g} Raman active modes of PtSe₂, respectively. The E_g mode is an in-plane vibrational mode of Se atoms moving away from each other within the layer, while the A_{1g} mode is an out-of-plane vibration of Se atoms in opposing directions. There is also a small peak located at ~230 cm⁻¹ which can be attributed to a longitudinal oscillation (LO) mode, similar to those observed in HfS₂, ZrS₂ and CdI₂^{32, 33}. For PtS₂, three main peaks at about 307, 335, and 340 cm⁻¹ can be assigned to E_g^1 , A_{1g}^1 , and A_{2g}^1 phonon modes, respectively. On the basis of previously theoretical prediction and experimental observations³⁵, we know that these two out-of-plane modes, A_{1g}^1 and A_{2g}^1 are observable in the polarization-dependent Raman spectra of PtS₂, while their intensities are polarization-dependent. This phenomenon can also be found in our experiment as shown in Figure 1d, the difference is that the intensity disparity between these two modes are not as obvious as the previously reported results because the samples in our experiments are formed with fine grains, as verified by X-ray diffraction (XRD), transmission electron microscopy (TEM) and Scanning TEM (STEM), which will be elucidated in the following part. Furthermore, Raman mapping images (inset of Figure 1d) indicate that the overlap part of the PtSe₂ and PtS₂ sheet are well-separated, where the PtSe₂ sheet stacks on the top of the PtS₂ sheet. The crystal structures of PtS₂ and PtSe₂ films were further explored by XRD, as shown in Figure S1a. The layered PtS₂ and PtSe₂ film can be viewed as cleaved from the (0001) surface of the bulk PtS₂ and PtSe₂, where one Pt atom layer is sandwiched between two S or Se layers (PtS₂: JCPDS PDF No. 01-070-1140, PtSe₂: JCPDS PDF No. 01-088-2280). The main XRD diffraction peaks of PtSe₂ films are observed at about 17.6°, 34.6°, and 54.6°, which can be indexed to the (001), (002) and (003) crystal planes of PtSe₂, respectively, suggesting that PtSe₂ film grows along c-direction with (001) as bottom plane, which agrees very well with the previous report^{35,36}. Similar results were found for the PtS₂

film. It is noteworthy that the diffraction peaks of Pt (111) disappeared after selenization or sulfuration which indicates a complete conversion of Pt into PtSe₂ and PtS₂.

The X-ray photoelectron spectroscopy (XPS) was also used to determinate the elemental binding energies of PtS₂, PtSe₂ sheets, and their vertical heterojunctions, as shown in Figure 1e and Figure S1(b). XPS spectra of the Pt 4f, Se 3d and S 2p were acquired on the heterojunction region. The measurement results for the binding energies clearly demonstrate the formation of PtS₂ and PtSe₂. The peak positions at 54.39 and 55.19 eV correspond to the binding energy of Se²⁻. Besides, two other peaks located at 73.9 and 77.3 eV of Pt 4f spectrum can be assigned to the Pt 4f_{7/2} and Pt 4f_{5/2}. The peaks at 162.3 and 163.6 eV of S 2p spectrum are ascribed to binding energy of Pt-S bonds between adjacent Pt atoms and S-S bonds, respectively, similar to the previous reports^{36,37}. To check the purity of the materials, the corresponding Pt, S and Se element mapping images were measured by energy dispersive X-ray spectroscopy, as displayed in Figure 1f, which confirms that all the elements are homogeneously distributed throughout the entire structure.

To further assess the microstructure, crystallinity, and elemental composition of the as-grown PtS₂/PtSe₂ vertical heterojunctions, the samples were transferred onto copper grid using the poly(methyl methacrylate) (PMMA) assisted transfer method³⁸ and investigated by TEM and STEM, as shown in Figure S2. The low-magnification TEM image (Figure S2b) indicates that the PtSe₂ and PtS₂ nanosheets have good uniformity and continuity across the whole platelet. The inset in Fig. S2c shows the selected area electron diffraction (SAED) pattern of PtSe₂ nanosheet, which confirms the obtained sample is polycrystalline and the four distinguished red dashed circles are assigned to (001), (101), (111) and (201) planes with lattice spacings of 5.15, 2.77, 1.55 and 1.75 Å, respectively. The inset in Fig. S2d shows the SAED pattern of PtS₂ nanosheet, which confirms the obtained sample is polycrystalline and the four distinguished red dashed circles are assigned to (101), (102), (111) and (202) planes with lattice spacings of 2.61, 1.93, 1.65 and 1.29 Å, respectively. The high-resolution TEM (HRTEM) image of the PtSe₂ nanosheet in Figure S2e reveal clear lattice fringes with a lattice spacing of 0.287 nm corresponding to (101) facets of PtSe₂ nanosheet, while for the PtS₂ nanosheet, the lattice space is 0.261 nm as shown in Figure S2f.

To gain basic understanding of the electronic properties of the PtS₂/PtSe₂ heterojunctions, theoretical simulations were conducted using the Vienna ab initio simulation package. Details of the simulation process is shown in Methods. The atomic geometries for layered PtSe₂, PtS₂ and coupled structure are shown in Figure 2 a-c. The 1T phase is selected since it is the most stable structure. The thickness of 5L-PtSe₂ and 5L-PtS₂ are 27.6 Å and 24.4 Å, comparable to the experimental value of 2.7 nm for PtSe₂ and 2.5 nm for PtS₂, respectively. Distances between adjacent Pt atoms in PtSe₂ and PtS₂ are 3.74 Å and 3.58 Å, respectively. When modeling coupled structure of PtSe₂ and PtS₂, the lateral lattice parameter of PtS₂ is slightly expanded in order to fix in the unit cell. Both 5L PtSe₂ and PtS₂ in 1T phase are observed to be semiconductors in experiments^{29, 34, 36, 37}. Figure 2 d-f show the simulated band structures. 5L-PtSe₂ has an indirect bandgap of 0.21 eV. The conduction band minimum (CBM) is settled between Gamma and M point, while the valance band maximum (VBM) is slightly offset from Gamma point. 5L-PtS₂ is also a semiconductor with indirect bandgap of 0.89 eV. Calculated bandgaps are highly consistent with the experimental observation²⁷. For the band structure of coupled system shown in panel f, the calculated band structure is only 0.03 eV, which seems to indicate a much more metallic feature, corresponding to a wide spread wavelength range. The plotted bands are a mixture of states from both PtS₂ and PtSe₂, which cannot represent the electronic properties of PtS₂ or PtSe₂ layers separately. In order to give a better estimation of the bandgap for each type of material, the projected density of states (PDOS) for Pt and Se/S atoms are also shown adjacent to band structures. By comparing the PDOS before and after the coupling, it can be found that the bandgap of PtS₂ is shrunk to half of its original size. Part of the shrink is caused by changing the lattice parameter. The PDOS of PtSe₂ is almost unchanged, indicating a limited response to the coupling. Both PtSe₂ and PtS₂ layers in the coupled system are still semiconductors since clear bandgaps are present in the PDOS plot. The VBM of coupled system is contributed by the PtSe₂ while the CBM is contributed by PtS₂ as shown in Figure S3 of Supporting Information. The shift of energy level respecting to the vacuum level is shown in Figure 3a. The conduction and valence band positions of 5L PtS₂ is at around -5 eV and -5.9 eV, respectively, while, the conduction and valence band positions of 5L PtSe₂ is located at -4.81 eV and -5.01 eV, respectively. The bandgap of PtS₂ decreases by 0.36 eV when its lattice parameter is stretched to the value of PtSe₂.

The coupled system has its conduction band and valence band slightly lifted up from their original levels, creating a tiny bandgap of 0.03 eV.

To further determine the band offset at the PtS₂/PtSe₂ interface, we performed ultraviolet photoelectron spectroscopy (UPS) measurements to test the band edge energies (Supporting Information, Figure S4). The results show that PtS₂ exhibits a higher work function (~ 4.99 eV) than that of PtSe₂ (~ 4.93 eV). The work function offset (60 meV) between PtS₂ and PtSe₂ should block electron flow from the PtS₂ film to the PtSe₂ film after contact. Note that the work functions derived from UPS measurements results may deviate from actual values because the material is etched by Ar ion-beam before UPS characterization (see supporting information Figure S4 for details). Recent research results have shown that the bandgap of PtSe₂ can be efficiently changed through defect engineering via Ar plasma treatment³³. The influence of plasma treatment on work function needs further investigation, which is out of the scope of this study. To this regard, kelvin probe force microscopy (KPFM) measurements were also performed to evaluate the energy offset at the PtS₂/PtSe₂ heterojunction interface and identify direction of the photocarriers transportation. The representative KPFM image under illumination of white light is shown in Figure S5a of Supporting Information. Figure S5b shows the corresponding surface potential taken along the dashed line in Figure S5a. The surface potential of the PtS₂ film is lower than that of the PtSe₂ film, which manifests PtS₂ has higher work function than PtSe₂. The work function difference between the two materials is approximately 35 meV (blue dashed line in Figure S5a). This disparity with UPS measurements result (60 meV) is because of the different environment in measurement (*i.e.* in air for KPFM measurement and in vacuum for UPS measurement), and defect induced bandgap change via Ar plasma treatment (as elucidated above). Combined with our theoretical calculation results, the schematic band diagrams in 5L PtS₂/5L PtSe₂ heterojunction can be depicted, as shown in Figure 3b. After contact, the Fermi levels in these two materials are shifted so as to satisfy the equilibrium condition due to the work function mismatch^{39, 40}. The electrons diffuse from PtSe₂ to PtS₂ and forms a built-in electric field, which leads to band bending between these two materials and facilitates separation of photo-excited carriers. Figure 3b also illustrates the transfer of photo-excited electron-hole pairs under light illumination. It is proposed that at least three processes can contribute to the photocurrent. The

photogenerated electrons in PtSe₂ at the interface of heterojunction are swept into PtSe₂ by the built-in electric field, while holes are blocked by the high barrier and accumulate at the interface. PtS₂ can also absorb light and generate electron-hole pairs. Moreover, carriers in the conduction band of the PtS₂ may be injected into PtSe₂, which will contribute more electrons to increase the photocurrent.

Figure 3c, d show the schematic illustration of a photodetector based on the PtS₂/PtSe₂ heterostructure and the corresponding current-voltage (*I-V*) characteristics in dark and under illumination. The device shows typical junction characteristics as seen from Figure 3d. At positive bias voltage, the current gradually enhances with the applied voltage (V_{SD}) due to the increase of carrier density. Furthermore, we found that the device can operate at no applied bias under infrared light illumination (1064 nm), as seen from Figure 3d and Figure 3e. Figure 3e shows the typical photocurrent switching performance of the heterostructure at the infrared wavelength of 1064 nm ($V_{SD} = 0$ V, $V_G = 0$ V). Obvious photoresponse is observed under different laser powers. This kind of self-powered operation behavior can have large numbers of applications like powerless communications, biological and chemical imaging in a wireless healthcare platform, and so on. A rectification ratio in the range of 15~20 was found for dozens of devices we have measured, which is similar with the values in recently reported TMDs-based junctions^{31, 41, 42, 43}. Furthermore, this relative weak rectifying behaviour indicates thermionic and/or tunneling electron currents can be present in our heterojunction.

Responsivity is an important figure of merit for a photodetector and reflects its sensitivity to the incident light. In order to normalize the incident power by the active area of the device, here we consider that the active area is the overlap region of the heterojunction, the responsivity ($R = I_{photo}/P_{incident}$, I_{photo} is the photocurrent and $P_{incident}$ is the incident power on the device active area) can be obtained. Figure 3f shows the dependence of photocurrent and responsivity on incident light power at zero-volt state. The photocurrent increases linearly while promoting the light power, while the responsivity decreases as the increase of incident power, in consistant with the behaviors of other TMDs-based heterojunctions reported before^{24,44}.

With the aim to demonstrate the capability of the broadband light detection of our device, a series of photoelectric measurements were performed at different wavelengths.

The temporal photoresponse with various wavelengths under the same light power (15 mW) is shown in Figure 4a. The device can be effectively switched ON and OFF while the light source is turned on and off even in the wavelength of 2200 nm (See the power-dependent photoresponse at 2200 nm in Figure S6, Supporting information). Moreover, the spectral photoresponse of the junction (Figure 4b) generally follows the absorption spectrum of 5L PtSe₂. The wavelength-dependent responsivity (Figure 4c) under the same light power shows a maximum at visible light illumination of 532 nm (15 mW) and then decreases as the photon energy decreases. The external quantum efficiency (EQE) represents the ratio of the number of collected charge carriers to the number of incident photons. It can be calculated by the formula $EQE = I_{photo} / P_{incident} (\hbar c / e \lambda)$, where λ is the incident wavelength, e is the electronic charge, \hbar is planck constant, c is the speed of light^{15, 17}. The EQE values as a function of wavelength are shown in Supporting Information Figure S7a. EQE is calculated to be around 7.1% at 1064 nm, 1.2% at 1550 nm and 0.2% at 2200 nm. Note that these EQE values may be overestimated since we considered only the overlap region of the heterojunction absorbs light. However, we found that if we consider the active area to be the entire semiconducting region, the calculated EQE values decreases by a factor of six, that is 1.2% at 1064 nm, 0.2% at 1550 nm and 0.05% at 2200 nm, which are the lower bounds for the EQE.

We further investigate the response speed of PtS₂/PtSe₂ heterojunction photodetector by shining the device with pulsed light that is modulated by an optical chopper as shown in Figure 4d. The response of the heterojunction is very fast with the rise and decay times to be 66 ms and 75 ms, respectively (Supporting Information, Figure S10a). The photoresponse of the PtS₂/PtSe₂ heterojunction remains highly stable after 60 days under the same illumination conditions, showing the excellent stability of the device in air at room temperature (Supporting Information, Figure S10b), which is very important for the practical implementation of this device in long-term operation. The performance of our PtS₂/PtSe₂ heterojunction devices is compared to other TMDs-based heterojunctions, as summarized in Table 1. The overall performance of our device is superior to existing MX₂/MX₂ (M = Mo, W; X = S, Se, Te) heterostructures in terms of working spectral range with comparable response time. We attribute the excellent photoresponse of PtS₂/PtSe₂ heterostructure to the small bandgap and enhanced light absorption in the coupled system.

Note that the 2D material quality remains far from optimal as evidenced from the TEM measurements, the response time of the hybrid system is only comparable to pristine PtS₂ photodetector, which is mainly limited by the existence of trap states³⁴, and may be further improved by optimizing the material quality and growth process.

CONCLUSION

In summary, wafer-scale 2D heterojunctions based on few-layer PtS₂ and PtSe₂ film were produced on a 2" SiO₂/Si substrate. Theoretical calculation along with the KPFM, UPS experimental verification were conducted to evaluate the electronic properties of the PtS₂/PtSe₂ heterojunction. Zero-bias photoresponse in the heterojunctions is observed under laser illumination of different wavelengths. The self-driven PtS₂/PtSe₂ heterojunctions show excellent characteristics in terms of wide photoresponse range from 405 to 2200 nm, high EQE at infrared wavelengths and a fast response speed. The speed of the device may be further improved by optimizing the material quality and growth process. The results demonstrated in this work may open up more possibilities toward infrared optoelectronic applications based on 2D materials.

METHODS

Synthesis of the PtS₂/PtSe₂ heterojunctions.

A two-step chemical vapor deposition approach was used to produce wafer-scale PtS₂/PtSe₂ heterojunctions in a double heating area furnace, similar to our previous report²⁴. In step one, photoresist was first spin-coated on the SiO₂/Si substrate and exposed to form the array of periodic square holes. Subsequently, 0.8 nm Pt was deposited by electron beam evaporation to the corresponding square holes. Then the SiO₂/Si substrate with Pt was placed into the quartz tube at the downstream and heated to 600 °C and sulfur powder was then put at the upstream with 130 °C. Argon (Ar) was introduced as the carrier gas (flow rate: 60 sccm). The SiO₂/Si substrates with Pt was maintained at 600 °C for 2 hours to form PtS₂. In step two, photoresist was spin-coated on the SiO₂/Si substrate with PtS₂ array and exposed again to form the periodic rectangle hole array on part of the PtS₂ sheets. After that, 0.8 nm Pt was then deposited by electron beam evaporation to form the periodic rectangle Pt arrays. Following, similar to the process of producing PtS₂ mentioned above,

the furnace temperature was kept at 450 °C for 2 hours to prepare PtSe₂.

Fabrication of the PtS₂/PtSe₂ heterojunctions devices.

UV lithography was used to define the source-drain electrodes pattern onto the PtS₂/PtSe₂ heterojunctions and then 5 nm Ti/80 nm Au was deposited through electron beam evaporation technique to form the source-drain electrodes.

Characterization of PtS₂/ PtSe₂ heterojunctions.

The morphology and structure of the synthesized materials were characterized by optical microscopy (OM, Olympus DX51), scanning electron microscopy (SEM, (FEI Quanta 200 FEG, acceleration voltage: 5 30 kV)), atomic force microscopy (AFM, Digital Instrument Nanoscope IIIA), transmission electron microscopy (TEM, FEI Tecnai F30, acceleration voltage: 200 kV), and micro-Raman spectroscopy (Horiba, LabRAM HR-800). X-ray photoelectron spectroscopy (XPS) measurement was performed on a KRATOS AXIS Ultra DLD equipment (KRATOS Analytical C.O.). Photoelectric measurements were performed on a probe station (Cascade M150) equipped with a semiconductor property analyzer (Kiteley 4200) in ambient conditions. More photoelectrical properties of the devices are described in the Supporting Information.

Simulations of the energy band of the PtS₂ and PtSe₂.

Simulations were conducted using the Vienna ab initio simulation package⁴⁵. The wave function was described by a plane-wave basis set with projected augmented wave method^{46,47}. The exchange-correlation functional was simulated with the optB86b exchange function⁴⁸ and van der Waals density functional method^{49,50}, which was found to be accurate in reproducing layered structures^{29, 51-53}. Energy cutoff for the plane wave basis was set to 400 eV in structural relaxations and increased to 500 eV in static calculations. Layered PtSe₂ and PtS₂ were modeled by a 1 × 1 supercell. 5L slab model was used for each type of materials, with a vacuum space of at least 20 Å in z direction. The k-mesh was sampled by a 3 × 3 × 1 k-mesh, accuracy tested by a 5 × 5 × 1 one. All atoms were relaxed until the residual force for each atom was less than 0.01 eV·Å⁻¹.

ACKNOWLEDGMENTS

We acknowledge the financial support from National Key Research & Development Program (No. 2016YFA0201902), the National Natural Science Foundation of China (No.

61604102, 51290273 and 11404372), ARC (DP140101501 and FT150100450), the Priority Academic Program Development of Jiangsu Higher Education Institutions (PAPD) and Collaborative Innovation Center of Suzhou Nano Science and Technology. Q. Bao acknowledges support from the Australian Research Council Centre of Excellence in Future Low-Energy Electronics Technologies (FLEET) (project number: CE170100039).

ASSOCIATED CONTENT

Supporting Information. Details of the XRD spectra, XPS spectra, TEM images, UPS and KPFM measurements results, and supplementary photoelectrical results at 2200 nm, 532 nm and 1064 nm are provided. This material is available free of charge on the ACS Publication website at <http://pubs.acs.org>.

AUTHOR INFORMATION

Corresponding Author

Shenghuang Lin and Shaojuan Li

Tel: (+86)-512-65882337; Fax: (+86)-512-65880820; E-mail:

shenghuanglinchina@gmail.com; sjli@suda.edu.cn

Author Contributions

Jian Yuan, Tian Sun and Zhixin Hu contributed equally to this work. The manuscript was written through contributions of all authors. All authors have given approval to the final version of the manuscript.

REFERENCES

1. Kroemer, H., A proposed class of hetero-junction injection lasers. *Proceedings of the IEEE* **1963**, 51, 1782-1783.
2. Gong, X.; Tong, M.; Xia, Y.; Cai, W.; Ji, S. M.; Cao, Y.; Yu, G.; Shieh, C. L.; Nilsson, B.; Heeger, A. J., High-Detectivity Polymer Photodetectors with Spectral Response from 300 nm to 1450 nm. *Science* **2009**, 325, 1665-1667.
3. Mueller, T.; Xia, F.; Avouris, P., Graphene photodetectors for high-speed optical communications. *Nat. Photonics* **2010**, 4, 297-301.
4. Lee, C. H.; Lee, G. H.; Zande, A. M. V. D.; Chen, W.; Li, Y.; Han, M.; Cui, X.; Arefe, G.; Nuckolls, C.; Heinz, T. F., Atomically thin p-n junctions with van der Waals heterointerfaces. *Nat. Nanotechnol.* **2014**, 9, 676-681.
5. Britnell, L.; Ribeiro, R. M.; Eckmann, A.; Jalil, R.; Belle, B. D.; Mishchenko, A.; Kim, Y. J.; Gorbachev, R. V.; Georgiou, T.; Morozov, S. V., Strong light-matter interactions in heterostructures of atomically thin films. *Science* **2013**, 340, 1311-1314.
6. Geim, A. K.; Grigorieva, I. V., Van der Waals heterostructures. *Nature* **2013**, 499, 419-425.
7. Ahmad, N.; Younus, H. A.; Chughtai, A. H.; Verpoort, F., Metal-organic molecular cages: applications of biochemical implications. *Chem. Soc. Rev.* **2015**, 44, 9-25.
8. Lin, S.; Liu, S.; Yang, Z.; Li, Y.; Ng, T. W.; Xu, Z.; Bao, Q.; Hao, J.; Lee, C. S.; Surya, C., Solution-Processable Ultrathin Black Phosphorus as an Effective Electron Transport Layer in Organic Photovoltaics. *Adv. Funct. Mater.* **2016**, 26, 864-871.
9. Lin, S.; Chui, Y.; Li, Y.; Shu, P. L., Liquid-phase exfoliation of black phosphorus and its applications. *Flatchem.* **2017**, 2, 15-37.
10. Chhowalla, M.; Shin, H. S.; Eda, G.; Li, L. J.; Loh, K. P.; Zhang, H., The chemistry of two-dimensional layered transition metal dichalcogenide nanosheets. *Nat. Chem.* **2013**, 5, 263-275.
11. Xu, Z. Q.; Zhang, Y.; Wang, Z.; Shen, Y.; Huang, W.; Xia, X.; Yu, W.; Xue, Y.; Sun, L.; Zheng, C., Atomically thin lateral p-n junction photodetector with large effective detection area. *2D Mater.* **2016**, 3, 041001.
12. Ghorbaniasl, M.; Kuc, A.; Miró, P.; Heine, T., A Single-Material Logical Junction Based on 2D Crystal PdS₂. *Adv. Mater.* **2016**, 28, 853-856.
13. Li, P.; Li, L.; Zeng, X. C., Tuning the electronic properties of monolayer and bilayer PtSe₂ via strain engineering. *J. Mater. Chem. C* **2016**, 4, 3106-3112.
14. Deng, Y.; Luo, Z.; Conrad, N. J.; Liu, H.; Gong, Y.; Najmaei, S.; Ajayan, P. M.; Lou, J.; Xu, X.; Ye, P. D., Black phosphorus-monolayer MoS₂ van der Waals heterojunction p-n diode. *ACS Nano* **2014**, 8, 8292-8299.
15. Furchi, M. M.; Pospischil, A.; Libisch, F.; Burgdörfer, J.; Mueller, T., Photovoltaic Effect in an Electrically Tunable van der Waals Heterojunction. *Nano Lett.* **2014**, 14, 4785-4791.
16. Cheng, R.; Li, D.; Zhou, H.; Wang, C.; Yin, A.; Jiang, S.; Liu, Y.; Chen, Y.; Huang, Y.; Duan, X., Electroluminescence and photocurrent generation from atomically sharp WSe₂/MoS₂ heterojunction p-n diodes. *Nano Lett.* **2014**, 14, 5590-5597.
17. Pezeshki, A.; Shokouh, S. H. H.; Nazari, T.; Oh, K.; Im, S., Electric and Photovoltaic Behavior of a Few-Layer α -MoTe₂/MoS₂ Dichalcogenide Heterojunction. *Adv. Mater.* **2016**, 28, 3216-3222.

18. Roy, T.; Tosun, M.; Hettick, M.; Ahn, G. H.; Hu, C.; Javey, A., 2D-2D tunneling field-effect transistors using WSe₂/SnSe₂ heterostructures. *Appl. Phys. Lett.* **2016**, 108, 083111.
19. Jo, S.; Ubrig, N.; Berger, H.; Kuzmenko, A. B.; Morpurgo, A. F., Mono- and bilayer WS₂ light-emitting transistors. *Nano Lett.* **2014**, 14, 2019-2025.
20. Amani, M.; Burke, R. A.; Proie, R. M.; Dubey, M., Flexible integrated circuits and multifunctional electronics based on single atomic layers of MoS₂ and graphene. *Nanotechnol.* **2015**, 26, 115202.
21. Liu, N.; Tian, H.; Schwartz, G.; Tok, J. B.; Ren, T. L.; Bao, Z., Large-area, transparent, and flexible infrared photodetector fabricated using P-N junctions formed by N-doping chemical vapor deposition grown graphene. *Nano Lett.* **2014**, 14, 3702-3708.
22. Zhang, Y. J.; Ye, J. T.; Yomogida, Y.; Takenobu, T.; Iwasa, Y., Formation of a stable p-n junction in a liquid-gated MoS₂ ambipolar transistor. *Nano Lett.* **2013**, 13, 3023-3028.
23. Pospischil, A.; Furchi, M. M.; Mueller, T., Solar-energy conversion and light emission in an atomic monolayer p-n diode. *Nat. Nanotechnol.* **2014**, 9, 257-261.24. Xue, Y.; Zhang, Y.; Liu, Y.; Liu, H.; Song, J.; Sophia, J.; Liu, J.; Xu, Z.; Xu, Q.; Wang, Z., Scalable Production of a Few-Layer MoS₂/WS₂ Vertical Heterojunction Array and Its Application for Photodetectors. *ACS Nano* **2016**, 10, 573-580.
25. Wang, Y.; Li, L.; Yao, W.; Song, S.; Sun, J.; Pan, J.; Ren, X.; Li, C.; Okunishi, E.; Wang, Y., Monolayer PtSe₂, a New Semiconducting Transition-Metal-Dichalcogenide, Epitaxially Grown by Direct Selenization of Pt. *Nano Lett.* **2015**, 15, 4013-4018.
26. Wang, Z.; Li, Q.; Besenbacher, F.; Dong, M., Facile Synthesis of Single Crystal PtSe₂ Nanosheets for Nanoscale Electronics. *Adv. Mater.* **2016**, 28, 10224-10229.
27. Zhao, Y.; Qiao, J.; Yu, P.; Hu, Z.; Lin, Z.; Lau, S. P.; Liu, Z.; Ji, W.; Chai, Y., Extraordinarily Strong Interlayer Interaction in 2D Layered PtS₂. *Adv. Mater.* **2016**, 28, 2399-2407.
28. Liu, Y.; Shivananju, B. N.; Wang, Y.; Zhang, Y.; Yu, W.; Xiao, S.; Sun, T.; Ma, W.; Mu, H.; Lin, S.; Zhang, H.; Lu, Y.; Qiu, C. W.; Li, S.; Bao, Q., Highly Efficient and Air-Stable Infrared Photodetector Based on 2D Layered Graphene-Black Phosphorus Heterostructure. *ACS Appl. Mater. Inter.* **2017**, 9, 36137-36145.
29. Zhao, Y.; Qiao, J.; Yu, Z.; Yu, P.; Xu, K.; Lau, S. P.; Zhou, W.; Liu, Z.; Wang, X.; Ji, W., High-Electron-Mobility and Air-Stable 2D Layered PtSe₂ FETs. *Adv. Mater.* **2017**, 29, 1604230.
30. Peng, Y. U.; Wang, Q.; Yu, X.; Liu, Z. In Mid-infrared 2D Photodetector based on bilayer PtSe₂, *CLEO: Science and Innovations. Optical Society of America*, **2016**; p STu4R.5.
31. Yim, C.; Mcevoy, N.; Riazimehr, S.; Schneider, D.; Gity, F.; Monaghan, S.; Hurley, P. K.; Lemme, M. C.; Duesberg, G. S., Wide spectral photoresponse of layered platinum diselenide based photodiodes. *Nano Lett.* **2018**, 18, 1794-1800.
32. Groenendijk, D. J.; Buscema, M.; Steele, G. A.; Michaelis de Vasconcellos, S.; Bratschitsch, R.; van der Zant, H. S. J.; Castellanos-Gomez, A., Photovoltaic and Photothermoelectric Effect in a Double-Gated WSe₂ Device. *Nano Lett.* **2014**, 14, 5846-5852.
33. Yu, X.; Yu, P.; Wu, D.; Singh, B.; Zeng, Q.; Lin, H.; Zhou, W.; Lin, J.; Suenaga, K.; Liu, Z.; Wang, Q. J., Atomically thin noble metal dichalcogenide: a broadband mid-infrared semiconductor. *Nat. Commun.* **2018**, 9, 1545.

34. Li, L.; Wang, W.; Chai, Y.; Li, H.; Tian, M.; Zhai, T., Few - Layered PtS₂ Phototransistor on h - BN with High Gain. *Adv. Funct. Mater.* **2017**, 27, 1701011.
35. O'Brien, M.; Mcevoy, N.; Motta, C.; Zheng, J. Y.; Berner, N. C.; Kotakoski, J.; Elibol, K.; Pennycook, T. J.; Meyer, J. C.; Yim, C., Raman Characterization of Platinum Diselenide Thin Films. *2D Mater.* **2016**, 3, 021004.
36. Chia, X.; Adriano, A.; Lazar, P.; Sofer, Z.; Luxa, J.; Pumera, M., Layered Platinum Dichalcogenides (PtS₂, PtSe₂, and PtTe₂) Electrocatalysis: Monotonic Dependence on the Chalcogen Size. *Adv. Funct. Mater.* **2016**, 26, 4306-4318.
37. Lin, S.; Liu, Y.; Hu, Z.; Lu, W.; Mak, C. H.; Zeng, L.; Zhao, J.; Li, Y.; Yan, F.; Tsang, Y. H.; Zhang, X.; Lau, S. P., Tunable active edge sites in PtSe₂ films towards hydrogen evolution reaction. *Nano Energy* **2017**, 42, 26-33.
38. Xu, Z. Q.; Zhang, Y.; Lin, S.; Zheng, C.; Zhong, Y. L.; Xia, X.; Li, Z.; Sophia, P. J.; Fuhrer, M. S.; Cheng, Y. B., Synthesis and Transfer of Large-Area Monolayer WS₂ Crystals: Moving Toward the Recyclable Use of Sapphire Substrates. *ACS Nano*, **2015**, 9, 6178-6187.
39. Kang, J.; Tongay, S.; Zhou, J.; Li, J.; Wu, J., Band offsets and heterostructures of two-dimensional semiconductors. *Appl. Phys. Lett.* **2013**, 102, 012111.
40. Li, S. L.; Komatsu, K.; Nakaharai, S.; Lin, Y. F.; Yamamoto, M.; Duan, X.; Tsukagoshi, K., Thickness Scaling Effect on Interfacial Barrier and Electrical Contact to Two-Dimensional MoS₂ Layers. *ACS Nano* **2014**, 8, 12836-12842.
41. Chen, K.; Wan, X.; Xie, W.; Wen, J.; Kang, Z.; Zeng, X.; Chen, H.; Xu, J., Lateral Built-In Potential of Monolayer MoS₂-WS₂ In-Plane Heterostructures by a Shortcut Growth Strategy. *Adv. Mater.* **2015**, 27, 6431-6437.
42. Howell, S. L.; Jariwala, D.; Wu, C. C.; Chen, K. S.; Sangwan, V. K.; Kang, J.; Marks, T. J.; Hersam, M. C.; Lauhon, L. J., Investigation of Band-Offsets at Monolayer-Multilayer MoS₂ Junctions by Scanning Photocurrent Microscopy. *Nano Lett.* **2015**, 15, 2278-2284.
43. Murthy, A. A.; Stanev, T. K.; Cain, J. D.; Hao, S.; LaMountain, T.; Kim, S.; Speiser, N.; Watanabe, K.; Taniguchi, T.; Wolverson, C.; Stern, N. P.; Dravid, V. P., Intrinsic Transport in 2D Heterostructures Mediated through h-BN Tunneling Contacts. *Nano Lett.* **2018**, 18, 2990-2998.
44. Wang, L.; Jie, J.; Shao, Z.; Zhang, Q.; Zhang, X.; Wang, Y.; Sun, Z.; Lee, S. T., MoS₂/Si Heterojunction with Vertically Standing Layered Structure for Ultrafast, High - Detectivity, Self-Driven Visible-Near Infrared Photodetectors. *Adv. Funct. Mater.* **2015**, 25, 2910-2919.
45. Kresse G, Furthmüller J., Efficient iterative schemes for *ab initio* total-energy calculations using a plane-wave basis set. *Phys. Rev. B* **1996**, 54, 11169.
46. Blöchl, P. E., Projector Augmented-Wave Method. *Phys. Rev. B* **1994**, 50, 17953-17979.
47. Kresse, G.; Joubert, D., From ultrasoft pseudopotentials to the projector augmented-wave method. *Phys. Rev. B* **1999**, 59, 1758-1775.
48. Klimeš, J.; Bowler, D. R.; Michaelides, A., Van der Waals density functionals applied to solids. *Phys. Rev. B* **2011**, 83, 195131.
49. Dion, M.; Rydberg, H.; Schröder, E.; Langreth, D. C.; Lundqvist, B. I., van der Waals density functional for general geometries. *Phys. Rev. Lett.* **2004**, 92, 246401.
50. Lee, K.; Murray, É. D.; Kong, L.; Lundqvist, B. I.; Langreth, D. C., A Higher-Accuracy van der Waals Density Functional. *Phys. Rev. B* **2010**, 82, 081101.

51. Hong, J.; Hu, Z.; Probert, M.; Li, K.; Lv, D.; Yang, X.; Gu, L.; Mao, N.; Feng, Q.; Xie, L., Exploring atomic defects in molybdenum disulphide monolayers. *Nat. Commun.* **2015**, 6, 6293.
52. Qiao, J.; Kong, X.; Hu, Z. X.; Yang, F.; Ji, W., High-mobility transport anisotropy and linear dichroism in few-layer black phosphorus. *Nat. Commun.* **2014**, 5, 4475.
53. Wu, J. B.; Hu, Z. X.; Zhang, X.; Han, W. P.; Lu, Y.; Shi, W.; Qiao, X. F.; Ijäs, M.; Milana, S.; Ji, W., Interface Coupling in Twisted Multilayer Graphene by Resonant Raman Spectroscopy of Layer Breathing Modes. *ACS Nano* **2015**, 9, 7440-7449.

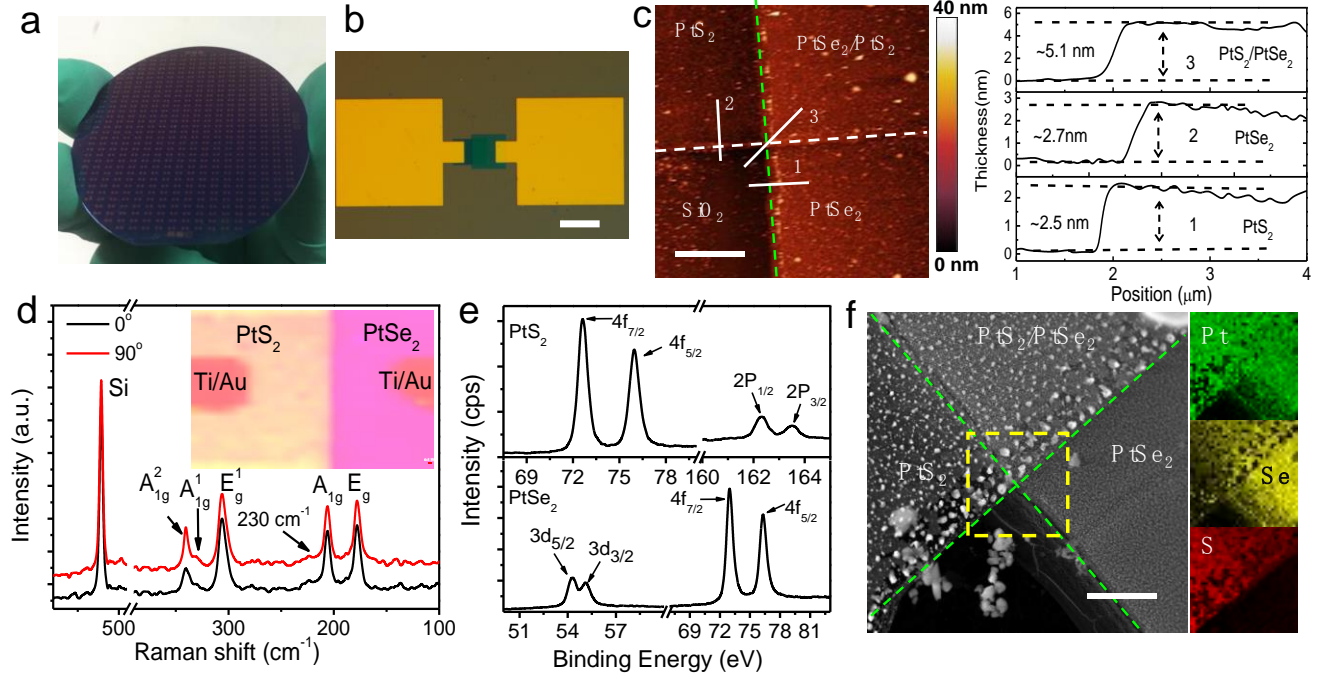


Figure 1. Material characterizations of the $\text{PtS}_2/\text{PtSe}_2$ heterojunctions. (a) The microscope image of $\text{PtS}_2/\text{PtSe}_2$ heterojunctions obtained on a 2" SiO_2/Si wafer with 300 nm thick silicon dioxide. (b) The high magnification microscope image of $\text{PtS}_2/\text{PtSe}_2$ heterojunction device. Scale bar: 100 μm . (c) The AFM image and profile of $\text{PtS}_2/\text{PtSe}_2$ heterojunction. Scale bar: 5 μm . (d) The Raman spectra of $\text{PtS}_2/\text{PtSe}_2$ heterojunction. Inset: The corresponding Raman mapping image. (e). The high-resolution XPS spectra of PtS_2 and PtSe_2 film. (f) The bright-field STEM image of Pt, Se and S elements, respectively. Scale bar: 20 nm.

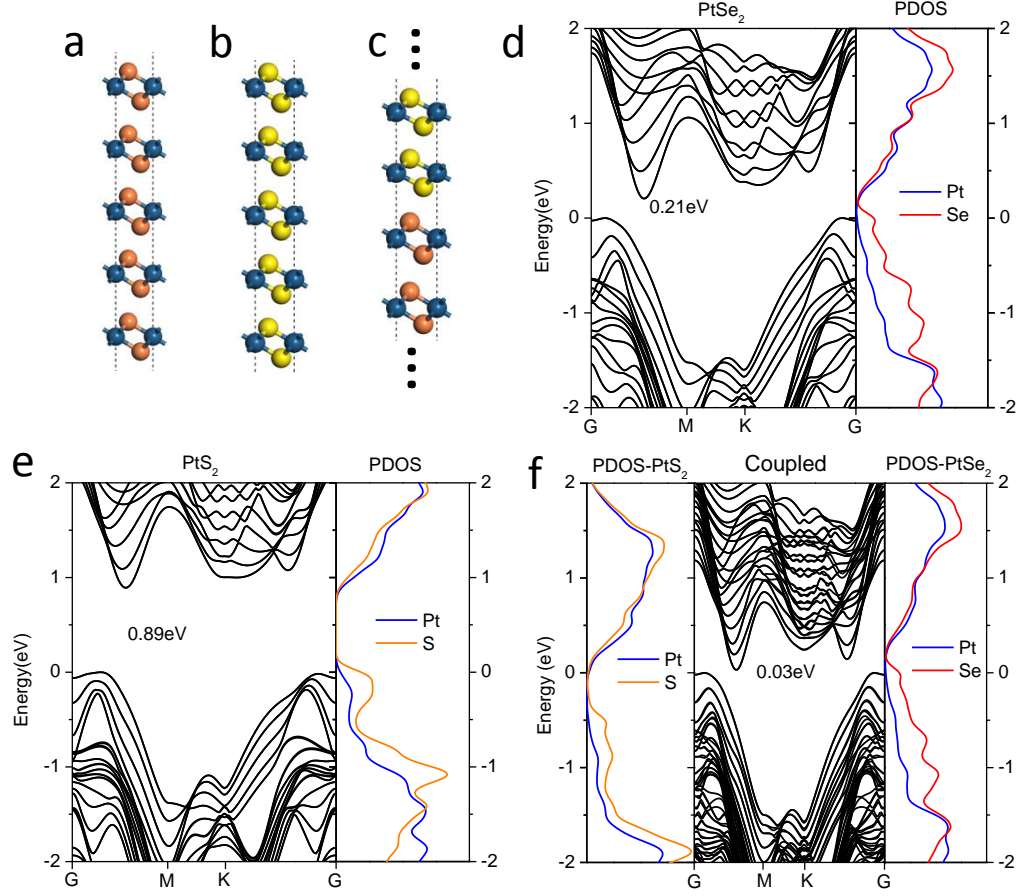


Figure 2. Simulations of the energy band of the PtS₂ and PtSe₂. (a-c) Atomic geometries and band structures of PtSe₂ and PtS₂. Blue, orange and yellow spheres in panel represent Pt, Se and S atoms respectively. 5L-PtSe₂ and 5L-PtS₂ are used in the coupled system in panel c. Some layers are not displayed in the figure in order to make the appearance clearer. The width of bandgap is inserted in band structure panels (d-f). Projected density of states (PDOS) for Pt and Se/S atoms are also shown adjacent to band structures.

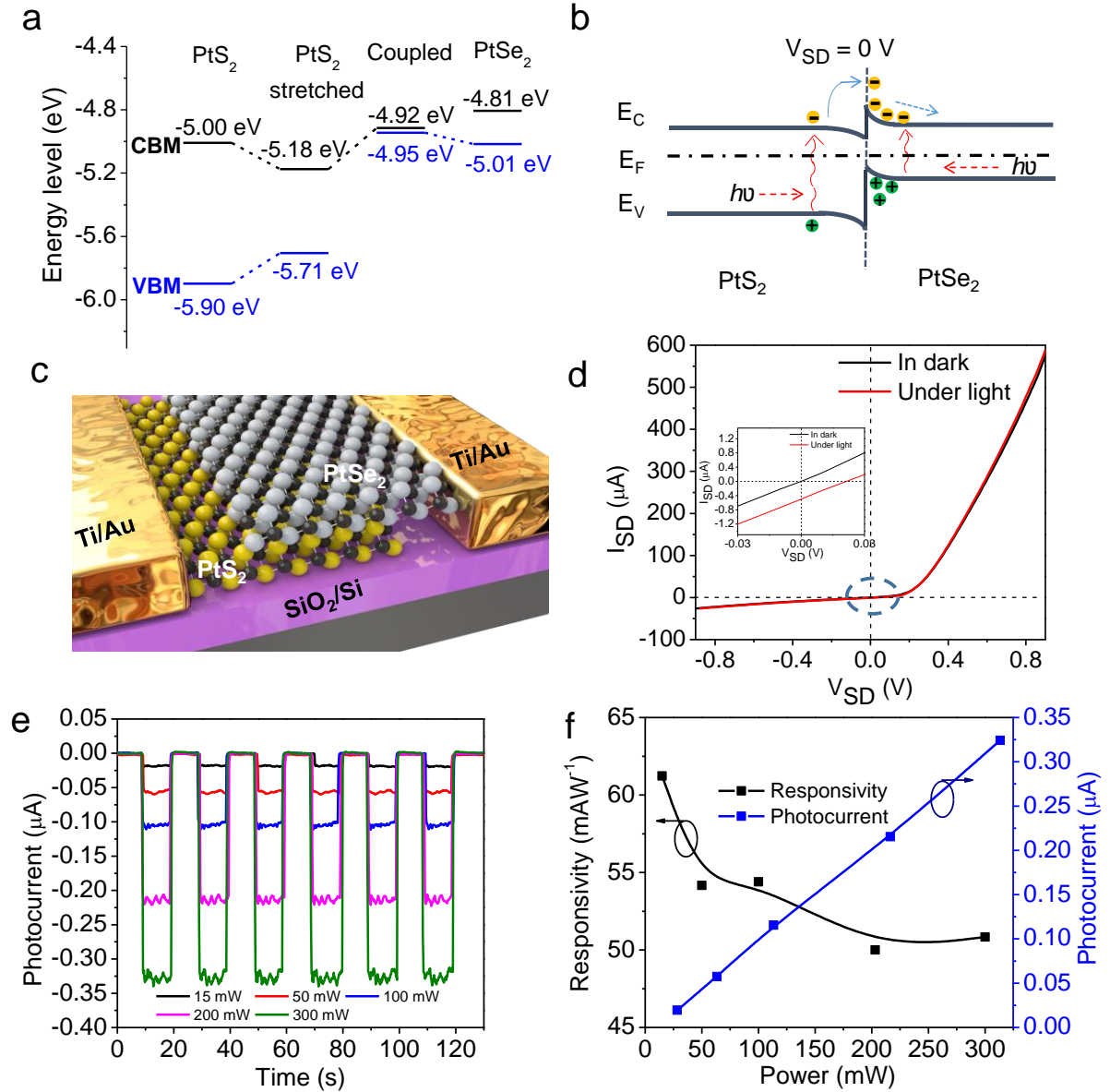


Figure 3. Energy diagrams and zero-bias photoresponse of the PtS₂/PtSe₂ heterojunctions. (a) Absolute energies of VBM (black) and CBM (blue) of PtS₂, PtSe₂ and the coupled structure. Dashed lines connecting those steps indicate the energy shift when the material is reshaped or coupled with other material. The column ‘PtS₂ stretched’ means lattice parameter of PtS₂ is stretched to adjust the value of PtSe₂. (b) Photoexcited carriers transfer process in the PtS₂/PtSe₂ heterojunctions under light illumination. E_C : conduction band; E_V : valence band. E_F : Fermi level. (c) Schematic illustration of a PtS₂/PtSe₂ heterojunction photodetector. (d) Representative I - V curves of the junction device at 1064 nm. Inset: Magnification image of I - V curves near zero bias voltage. (e) Time-dependent photocurrent

response exited under 1064 nm light illumination with different powers. (f) Dependence of photocurrent and responsivity on light power at 1064 nm. $V_{SD} = 0$ V, $V_G = 0$ V.

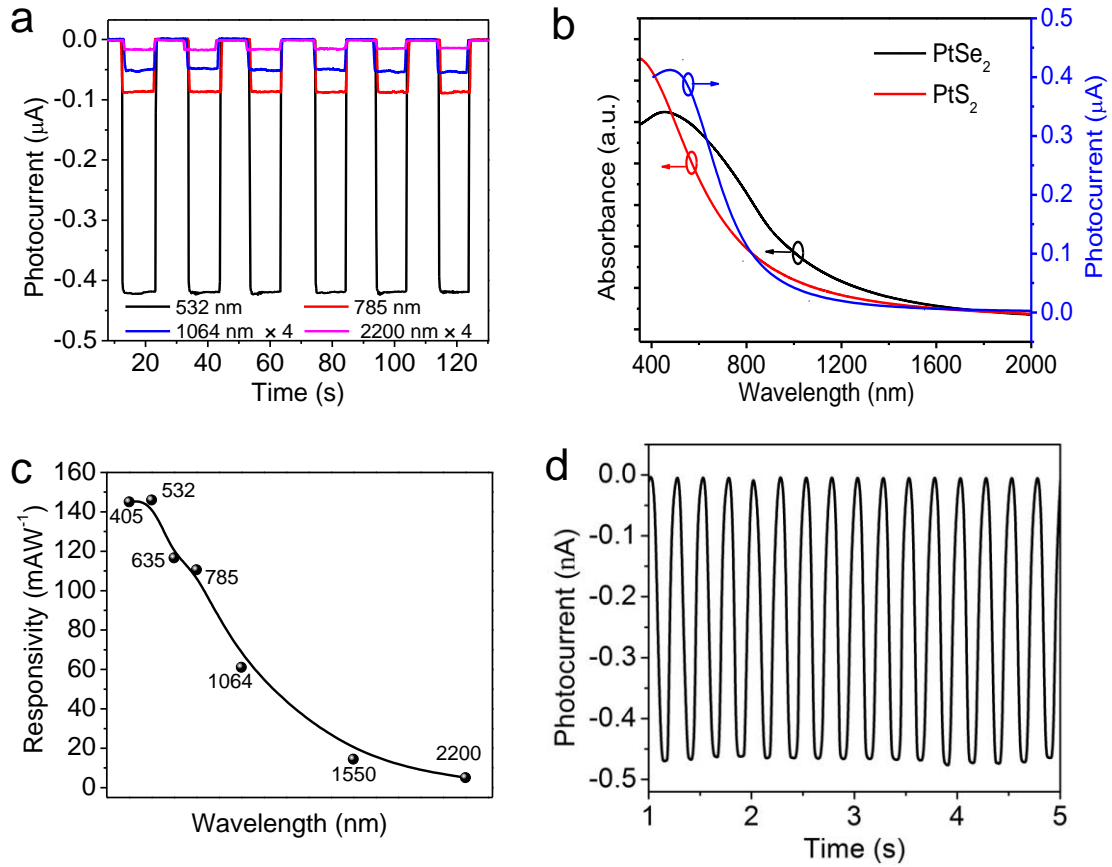


Figure 4. Broadband photoresponse of the PtS₂/PtSe₂ heterojunction devices. (a) The temporal photoresponse of the PtS₂/PtSe₂ heterojunctions with various wavelengths under the same light power (15 mW). $V_{SD} = 0$ V, $V_G = 0$ V. (b) The absorption spectrum of PtSe₂ and PtS₂ films and the corresponding wavelength-dependent photocurrent of the PtS₂/PtSe₂ heterojunction devices. (c) The wavelength-dependent responsivity under the same light power (15 mW). (d) Photoresponse of the PtS₂/PtSe₂ heterojunction devices to pulsed infrared light irradiation (1064 nm laser) with a frequency of 8 Hz. $V_{SD} = 0$ V, $V_G = 0$ V.

Table 1 Comparison of the performance of PtS₂/PtSe₂ heterojunction devices with previously reported TMDs/TMDs and TMDs/BP heterojunctions.

Materials	Measurement Conditions	Responsivity (mA/W)	EQE	Response time (ms)	Range of response wavelength (nm)	Reference
Multilayer MoS ₂ /WSe ₂	V _{sd} = 0 V 532 nm	~120	34%	*	500-800	<i>Ref.4</i>
BP/MoS ₂	V _{sd} = 0 V 633 nm	*	0.3%	*	*	<i>Ref.14</i>
Double gated MoSe ₂ PN junction	V _{sd} = -1 V 532 nm	0.7	0.1%	10 ms	400-800	<i>Ref.32</i>
MoTe ₂ /MoS ₂	V _{sd} = 0 V 405 nm 800 nm	322 38	88% 6%	25 ms	400-800	<i>Ref.17</i>
PtS ₂ /PtSe ₂	V _{sd} = 0 V 1064 nm 1500 nm 2200 nm	10.2 2.4 0.6	1.2 % 0.2 % 0.05%	66 ms	405-2200	<i>This work</i>